Plume Source Localization on Enceladus by Sequential Monte Carlo Method

Yue Sun*
Harbin Institute of Technology, 150001 Harbin, People's Republic of China
Alex Ellery†
Carleton University, Ottawa, Ontario K1S 5B6, Canada
and
Xianlin Huang‡
Harbin Institute of Technology, 150001 Harbin, People's Republic of China

https://doi.org/10.2514/1.A34982

Water vapor plumes emanating from the geyser vents at Enceladus's south pole area invite the possibility of direct access to the subsurface liquid reservoir to acquire pristine biological material if it exists. Any descending lander adapted for plume localization is required to not only explore the icy plume environment during its descent, but it must also infer the location of the landing target—the plume source—autonomously. Compared with existing scenarios of terrestrial plume source localization methods, the source likelihood map (SLIM) method for an Enceladus mission offers a more extensive search area, a higher maneuver velocity, and a shorter search time. This paper investigates a particle-based odor source localization (pOSL) approach that offers the prospect of targeting one of the plume sources by autonomously measuring the concentration field. Reasons for the negative likelihood and overfitting issues associated with Bayesian SLIM are analyzed to build a novel probabilistic model. By implementing this model, the proposed pOSL algorithm evaluates the observation likelihood via posterior maximization method and estimates the source location via the sequential Monte Carlo method. The pOSL algorithm resolves difficulties associated with other methods while reducing the time complexity from $O(N^{\tau})$ to $O(N)$. The numerical simulations illustrate that the proposed approach is feasible and permits accurate targeting of Enceladus's geyser vents.

Nomenclature

A	=	linear coefficient of a linear Gaussian model
b	=	bias of a linear Gaussian model
C_0	=	density at the center of the plume on Enceladus's surface, 2.7×10^9 cm^{-3}
c	=	concentration field (cm^{-3})
$\mathbb{E}$	=	expectation operator
H_d	=	four times the radius of Enceladus's Hill sphere, 3792 km
H_Θ	=	angular width of the plume, 12°
h	=	altitude (km)
k	=	dimension of the search area
L	=	precision matrix of a linear Gaussian model
N	=	maximum number of sampled particles
$\mathcal{N}$	=	normal distribution
N_{eff}	=	resampling flag
O	=	source location (m)
P	=	probability
R_E	=	radius of Enceladus, 248,329 m
r	=	plume center distance (m)
s	=	latent variable representing π
U	=	uniform distribution
V	=	covariance matrix of observation likelihood
x	=	lateral coordinates in cross-range direction (m) or measured concentration value (cm^{-3})
x_0	=	lateral coordinates of source in cross-range direction (m)
y	=	lateral coordinates in down-range direction (m)
y_0	=	lateral coordinates of source in down-range direction (m)
z	=	vehicle position (m)
α	=	learning rate of particle-based odor source localization algorithm
β	=	posterior distribution of source
$\hat{\beta}$	=	estimate of β
Γ	=	observation noise
γ	=	learning rate
Δ	=	plume model residual
Δt	=	sample time of robot system (s)
ΔV	=	impulses needed to perform a maneuver (m/s)
Θ	=	angular distance from the plume center (m)
Λ	=	precision matrix of a prior normal distribution
μ	=	expectation of observation likelihood
π	=	mixture factor
Σ	=	covariance matrix of plume model
σ	=	covariance matrix determined by wind field
τ	=	assumed releasing time of icy odors (s)
χ	=	observation event

Subscripts

n	=	index of sampled particles
t	=	time

Received 4 October 2020; revision received 16 November 2020; accepted for publication 21 December 2020; published online 25 January 2021.

*Doctoral Candidate, Centre of Control Theory and Guidance Technology, School of Astronautics, No. 92, Dazhi W Street; currently Visiting Doctoral Student, Mechanical and Aerospace Engineering Department, Carleton University, 1125 Colonel By Drive, Ottawa, Ontario K1S 5B6, Canada; yuesun8@cunet.carleton.ca.

†Professor, Mechanical and Aerospace Engineering Department, 1125 Colonel By Drive; alexellery@cunet.carleton.ca.

‡Professor, Centre of Control Theory and Guidance Technology, School of Astronautics, No. 92, Dazhi W Street; xlinhuang@hit.edu.cn.

I. Introduction

THE icy moons of the solar system represent the most promising targets for astrobiological exploration [1,2]. The water vapor plumes from Enceladus's south pole area discovered by the Cassini spacecraft and the implied subsurface salt-water reservoir [3] have attracted significant scientific attention [4]. Icy water particles and the water vapor gas gush from cryovolcanism in Enceladus's south

pole area (forming fissures known as tiger stripes area) continuously blanket Enceladus's surface, making the icy moon one of the most reflective bodies in the solar system [5]. These cryo-eruptions also supply material to replenish Saturn's E-ring [4]. The Cassini spacecraft performed dozens of flybys past Enceladus from 2005 to 2008, including 8 flybys near Enceladus's south pole area with the lowest flyby altitude being 50 km [6]. Cassini's measurements of the water plumes [7] reveal that there are liquid water oceans beneath a frozen shell of a thickness ∼10 km [8] and implies that submarine hydrothermal activity at the rocky core [9] might harbor the ingredients for life [10]. Emplacing scientific instruments into or near one of the plume sources to directly access water from the subsurface oceans would be a boon for astrobiological research [11]. To date, this has been considered too challenging [12]; it is this aspect that is addressed here.

To explore Enceladus's plume environment and to sample its subsurface astrobiological material [13], we propose that one or more penetrators explore the plume environment through lateral maneuvers to infer the location of the landing target during the descent [14]. The planetary penetrator is advocated as one of the most attractive vehicles for a small body targeting [15]. This small missile-type landing vehicle can carry modest scientific instruments and be capable of withstanding impact into the subsurface [16,17]. In contrast to previous lander missions [18,19], the precise location of an Enceladus landing target would be unknown a priori. Any Enceladus lander must explore the icy plume environment in situ to infer the location of the landing target (the plume vent) by employing source localization algorithms autonomously during its descent. Source likelihood map (SLIM) methods involve algorithms that exhibit animal-like food-foraging behavior, which incrementally map the plume by measuring the concentration field continuously. SLIM approaches for Enceladus are substantially different from existing terrestrial scenarios. Whether on the ground or underwater, the search area of existing algorithms is ∼100–200 m while the velocity of the mobile robot does not exceed ∼10 to 30 $\mathrm{m}\cdot\mathrm{s}^{-1}$. However, an Enceladus lander may intercept the plume at an altitude of ∼200–300 km with a lateral maneuvering corridor of ∼50–90 km diameter, which is over two orders of magnitude larger [20]. The velocities involved are also an order of magnitude larger because the required impact velocity of a penetrator is ∼100–300 $\mathrm{m}\cdot\mathrm{s}^{-1}$ dictated by the required subsurface penetration depth [14]. Consequently, an advanced SLIM method is crucial for Enceladus plume mapping and the exploration of subsurface targets of astrobiological interest.

Traditional SLIM methods implemented on mobile robots can be classified in different ways [21]. The most conventional methods are biologically inspired behavior-based approaches, including gradient search and infotaxis strategies. Gradient-based strategies [22] enable a mobile robot to trace a Gaussian plume field and locate the plume source via a gradient descent algorithm. Infotaxis strategies [23], including upwind search [24], SPIRAL search [25], and swarm search [26], are a type of non-Gaussian plume search method without using gradient information. Plume source localization via machine learning is also an attractive type of approach [27]. This approach defines the search area as a sequence of cells and allows the robot to learn a SLIM through the forward and backward recursive algorithm of a discrete hidden Markov model (HMM). A particle-filter-based SLIM can estimate the posterior expectation of source position by implementing a Gaussian likelihood function [28]. However, the likelihood function of this method may give negative likelihoods. Besides, the particle method is expensive requiring $O(N^{\tau})$ operations to evaluate the posterior expectation, where N is the number of particles and τ is the assumed released time. All the above approaches lose their effectiveness when addressing the scenario of a large three-dimensional search area with a high-velocity vehicle and a short descent duration; these are the constraints imposed by Enceladus plume mapping.

We have investigated a novel particle-based odor source localization (pOSL) approach that permits an Enceladus lander to locate the plume vents by sniffing the plume during the descent. This novel pOSL approach evaluates the observation likelihoods by the maximum a posteriori (MAP) method and estimates the posterior expectation of the source position using the sequential Monte Carlo (SMC) technique [29]. The proposed algorithm resolves the issues of traditional methods while reducing the time complexity from a polynomial function of $O(N^{\tau})$ to a linear function of $O(N)$. By employing the proposed approach, an Enceladus penetrator could precisely target Enceladus's geyser vents with a biomimetic decent behavior.

The following are the main contributions of this paper:

1) We propose a novel probability model for the odor source localization problem that avoids the negative likelihood and overfitting (NLO) issues, based on the analysis of the traditional OSL approaches in both discrete and continuous cases. By employing graphic models, we also indicate the reason for the NLO issue (Sec. II).

2) We develop a novel algorithm using the SMC method that corrects the deficiencies of traditional methods while reducing its time complexity (Sec. III).

3) We perform a penetrator mission concept to demonstrate the effectiveness of the proposed algorithm (Sec. IV).

II. Probabilistic Model That Avoids the NLO Issue

In this section, we briefly cover the HMM-based methods and the particle-filter-based method from the perspective of the Bayesian directed-graph model and expound the reasons for the NLO issue. We then propose a novel directed-graph model that could avoid the above issues.

A. Negative Likelihood and Overfitting Issues

1. *HMM-Based and Particle-Filter-Based Method*

Consider a mobile robot searching the plume source and locating the odor source by continuously measuring the concentration $\{\chi_1,\chi_2,\ldots,\chi_t\}$ at position $\{r_1, r_2,\ldots, r_t\}$ yielded by O. We give the directed-graph model of Fig. 1 that describes the HMM-based method [27] and the particle-filter-based method [28].

The traditional methods estimate posterior distribution of the source position β_t by

$$\beta_t = P(O|\,\chi_1 \sim \chi_t) = \frac{P(\chi_t|O)\beta_{t-1}}{\int P(\chi_t|O)\beta_{t-1}\,\mathrm{d}O} \tag{1}$$

where $\chi_t = \{\chi_t, r_t\}$ represents the detection events. The HMM-based method divides the search area into N cells and estimates β_t by the forward and backward recursion algorithm of a discrete HMM. This method calculates the likelihood by averaging the probabilities between $P(r_t|O_{t-\tau})$ to $P(r_t|O_t)$ [Eq. (2)], assuming that the detected odor is released at one of the time steps between $t-\tau$ and t.

$$P(\chi_t|O) = \begin{cases} \dfrac{1}{\tau}\displaystyle\sum_{t-\tau}^{t} P(r_t|O_t), & \chi_t = 1 \\ 1 - \dfrac{1}{\tau}\displaystyle\sum_{t-\tau}^{t} P(r_t|O_t), & \chi_t = 0 \end{cases} \tag{2}$$

This approach requires an expensive $O(N^3)$ matrix operations for each observation in 3D scenarios, which make it lose effectiveness when addressing Enceladus plume localization problem.

Assuming that χ_t is yielded by one or more time steps between $t-\tau$ and t, the particle-filter-based method defines the likelihood as

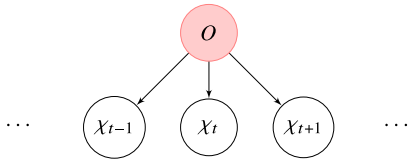

Fig. 1 Graphical model of the HMM-based method and the particle-filter-based method, where χ_t represents the detection events, and O is the source location.

$$P(\chi_t|O) = \begin{cases} 1 - \prod_{t-\tau}^{t} 1 - Q(r_t|O_t), & \chi_t = 1 \\ \prod_{t-\tau}^{t} 1 - Q(r_t|O_t), & \chi_t = 0 \end{cases}$$
$$Q(r_t|O_t) = \frac{1}{2\pi\sigma_x\sigma_y(\tau)\Delta t} e^{-\frac{(\delta_{ix}(l,k))^2}{2\sigma_x^2(\tau)\Delta t}} e^{-\frac{(\delta_{iy}(l,k))^2}{2\sigma_y^2(\tau)\Delta t}} \quad (3)$$

where Δt = sampling period and $[\sigma_x^2, \sigma_y^2]^T$ = variance of the components of the airflow. A particle filter is thus implemented to evaluate the expectation of $P(r_t|O)$, i.e., $\mathbb{E}\beta_t$. This algorithm imposes an expensive computational cost of $O(N^\tau)$, where N is the number of particles and τ is the release time. Furthermore, this approach has issues surrounding negative likelihood and overfitting.

2. Negative Likelihood Issue

According to Eq. (3), the maximum of $Q(r_t|O_t)$ is $1/\sqrt{(2\pi)^k|\Sigma|}$, where k denotes the dimension of the search area. The maxima will greater than 1 when $|\Sigma| < \left(1/\sqrt{(2\pi)^k}\right)$, resulting in a negative $1 - Q(r_t|O_t)$ and a negative $P(r_t|O)$.

The reason is as follows. Intuitively, the likelihood function should be proportional to the probability density. However, the likelihood function does not obey the condition of normativity; i.e., the mutually exclusive likelihood of an event A is not 1-likelihood(A), according to the law of complement. Besides, the graphic model (Fig. 1) also indicates that the uncertainties of the detection event cannot be transported from node χ_{t-1} to node χ_t with a transition distribution given by

$$P(\chi_t|O_t) = \begin{cases} Q(z^*|O_t), & r^* = r_t \\ 0, & r^* \neq r_t \end{cases}$$

3. Overfitting Issue

Worse still, the likelihood defined by Eq. (3) may cause the overfitting problem: when the robot detects $\chi_t = 1$ at r_t, the most likely source position is $O = r_t$ and if $\chi_t = 0$, the position farther from r_t is more likely to be O based on Eq. (3). Note that the exponential term of the Gaussian density in Eq. (3) is a quadratic function given by

$$-\frac{1}{2}(\boldsymbol{r_t} - \boldsymbol{O})^{\mathrm{T}}\Sigma^{-1}(\boldsymbol{r_t} - \boldsymbol{O}) \quad (4)$$

As shown in Fig. 2, the likelihood of a detected event $\chi_t = 1$ would increase when O is getting close to r_t, as $O = r_t$ is the maxima of the likelihood function. Equation (4) implies that the most likely source position given by Eq. (3) at r_t is r_t itself since $P(r_t|O)$ gets its maximum when $O = r_t$, and vice versa. In other words, if a particle filter with a likelihood function of Eq. (3) is implemented, particles around r_t are likely to attain large weights when $\chi_t = 1$ and to attain small weights when $\chi_t = 0$. This phenomenon may cause very strong overfitting, such that the convergence of the algorithm would be damaged. Although this is not a big problem when searching a small search area with a mobile robot, in scenarios like Enceladus plume mapping, the impact velocity of a landing vehicle is required to be high ~100–300 m · s^{-1} to guarantee an effective impact depth, leaving little time for lateral maneuvers to alter the impact target.

In Sec. II.B, we propose a novel probabilistic model that provides a more efficient mechanism to describe the probabilistic dynamics. This novel model also enables us to evaluate the likelihood via the MAP method that could avoid the aforementioned issues.

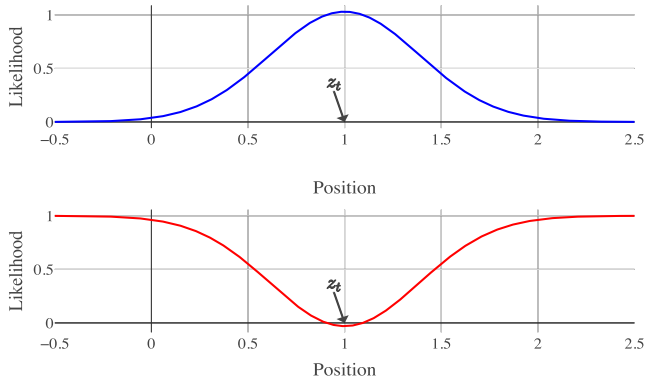

Fig. 2 One-dimensional schematic of overfitting. When $\chi_t = 1$, r_t is the most likely O, while the position farther from r_t is more likely to be O when $\chi_t = 0$.

B. Probabilistic Model of Particle-Based OSL Problem

Let $\{c_1, \ldots, c_t\}$ = the concentration value, and the novel probabilistic model given by Fig. 3 and Eq. (5) models the detection events, considering the plume model residual and the observation noise $\mathcal{N}(0, \Gamma)$.

$$P(c_t|O) \sim \mathcal{N}(c_t|\mathcal{C}(O, r_t), \Delta)$$
$$P(\chi_t|c_t) \sim \mathcal{N}(\chi_t|c_t, \Gamma) \quad (5)$$

The first equation of Eq. (5) defines the concentration value c_t at r_t predicted by a plume model $\mathcal{C}(*)$ with a residual Δ. Therefore the target variable O becomes a hyperparameter. Note that this model separates the nonlinear observation segment and the nonlinear plume model. The state-space form is given by

$$c_t = \mathcal{C}(O, r_t) + \Omega_t$$
$$\chi_t = c_t + \Lambda_t$$

where $\Omega_t = \mathcal{N}(0, \Delta)$ and $\Lambda_t = \mathcal{N}(0, \Gamma)$ are both white Gaussian noise.

By employing the concentration value as the hidden variable, the evaluation of the observation likelihood becomes a MAP problem, instead of a maximum likelihood estimation (MLE) problem. Thus the likelihood probability is capable of being proportional to the concentration value rather than being maximized. This would resolve both the overfitting issue and also the negative likelihood issue, because there are no mutually exclusive events in the proposed model. The probabilistic model also implies that the odor source localization problem is equivalent to a hyperparameter estimation problem given by

Problem 1: Estimate the posterior expectation of the hyperparameter O in model 5, $\mathbb{E}\beta_t$, where

$$\beta_t = P(O|\chi_0, \ldots, \chi_t)$$

The proposed probabilistic model suggests a novel odor SLIM method. In the next section, we evaluate the observation likelihood using the MAP method and estimate the posterior expectation of the source location via the SMC method. This novel algorithm avoids the negative likelihood and improves the overfitting while reducing the time complexity. We refer to this as the pOSL algorithm.

III. Particle-Based Odor Source Localization Method

Considering Bayes's theorem and the conditional independence principle, the joint distribution of all nodes in the graphic model is given by

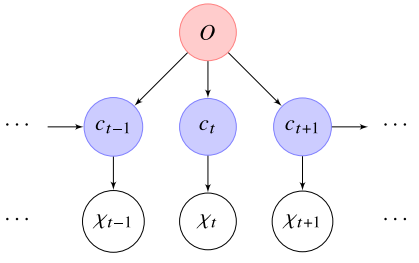

Fig. 3 Graphical model with model uncertainty, where O is a hyperparameter representing the source location, $\{c_1, \ldots, c_t\}$ is the concentration fields, and $\{\chi_1, \chi_2, \ldots, \chi_t\}$ is the observation.

$$
\begin{aligned}
P(c_1 \sim c_t, \chi_0 \sim \chi_t, O) &= P(c_1 \sim c_t, \chi_0, \ldots, \chi_t | O) P(O) \\
&= P(\chi_0, \ldots, \chi_t | c_1 \sim c_t) P(c_1 \sim c_t | O) P(O) \\
&= P(\chi_t | \chi_0 \sim \chi_{t-1}, c_1 \sim c_t) P(\chi_0 \sim \chi_{t-1} | c_1 \sim c_t) \\
&\quad P(c_t | c_1 \sim c_{t-1}, O) P(c_1 \sim c_{t-1} | O) P(O) \\
&= P(\chi_t | c_t) P(\chi_0 \sim \chi_{t-1} | c_1 \sim c_t) P(c_t | O) \\
&\quad P(c_1 \sim c_{t-1} | O) P(O) \\
&= P(O) \prod_1^t P(\chi_t | c_t) P(c_t | O) \qquad (6)
\end{aligned}
$$

implying that

$$
\begin{aligned}
&\beta_t P(\chi_t | \chi_1, \ldots, \chi_{t-1}) \\
&= P(O | \chi_1, \ldots, \chi_t) P(\chi_t | \chi_1, \ldots, \chi_{t-1}) \\
&= P(\chi_t | O) P(O | \chi_1, \ldots, \chi_{t-1}) \\
&= P(\chi_t | O) \beta_{t-1} \qquad (7)
\end{aligned}
$$

Based on Eq. (7), the pOSL algorithm estimates the posterior expectation of hyperparameter O by two steps: a MAP step and an SMC step. The MAP step evaluates the observation likelihood by solving $P(\chi_t|O) = \int P(\chi_t|c_t)P(c_t|O)\,\mathrm{d}c_t$, and the SMC step estimates $\mathbb{E}\beta_t$ via the SMC method.

A. Evaluation of the Observation Likelihood

Based on the graphic model, the likelihood $P(\chi_t|O)$ can be computed as a convolution by

$$
\begin{aligned}
P(\chi_t | O) &= \int P(\chi_t | c_t) P(c_t | O)\,\mathrm{d}c_t \\
&= \int \mathcal{N}(\chi_t | c_t, \Gamma) \mathcal{N}(c_t | f(O, r_t), \Delta)\,\mathrm{d}c_t \qquad (8)
\end{aligned}
$$

Using Lemma 1, the likelihood $P(\chi_t|O) = \mathcal{N}(\chi_t|\mu_t, V_t)$ is traceable, given by

$$
\begin{aligned}
&P(\chi_t | O) \sim \mathcal{N}(\chi_t | \mu_t, V_t) \\
&\mu_t = \mathcal{C}(O, r_t) \\
&V_t = \Delta + \Gamma \qquad (9)
\end{aligned}
$$

Lemma 1: Given a marginal Gaussian distribution for x and a Gaussian distribution for y on the conditional of x in the form [30]

$$
\begin{aligned}
&P(x) = \mathcal{N}(x | \mu, \Lambda^{-1}), \\
&P(y | x) = \mathcal{N}(y | Ax + b, L^{-1})
\end{aligned}
$$

the marginal distribution of y and x on the conditional of y are given by

$$
\begin{aligned}
&P(y) = \mathcal{N}(y | A\mu + b, L^{-1} + A\Lambda^{-1}A^T) \\
&P(x | y) = \mathcal{N}(x | \Sigma\{A^T L(y - b) + \Lambda\mu\}, \Sigma) \\
&\Sigma = (\Lambda + A^T L A)^{-1}
\end{aligned}
$$

For linear systems, a Kalman filter offers a closed-form solution of β_t in Eq. (7). For the nonlinear plume model, we implement the SMC method to evaluate the posterior expectation of β_t.

B. SMC-Based Estimation of the Posterior Expectation

1. Inference of $\mathbb{E}\beta_t$

The SMC method is a general class of the Monte Carlo method that samples sequentially from target probability densities to evaluate its posterior approximation expectation. By implementing the SMC method, Theorem 1 gives the posterior expectation of β_t.

Theorem 1: The posterior expectation of β_t in Problem 1 is

$$
\begin{aligned}
&\mathbb{E}\beta_t = \sum_{i=1}^{I} \omega_t^n O_{t-1}^n \\
&\theta_{t-1}^{*,n} \sim \beta_{t-1} \\
&\omega_t^n \propto P(\chi_t | O), \sum \omega_t^n = 1 \qquad (10)
\end{aligned}
$$

Proof: Assuming that one draws samples $O_{t-1}^n \sim \beta_{t-1}$ for $n = 1, \ldots, N$, the approximation of β_t is given by the empirical measure:

$$
\hat{\beta}_t \approx \sum_{n=1}^{N} P(\chi_t | O_{t-1}^n) \delta_{O_t^n}(O_{t-1}^n) \qquad (11)
$$

where $\delta_{O_t^n}(O_{t-1}^n)$ is the Dirac-delta function for O_t^n and O_{t-1}^n. $P(\chi_t|O_{t-1}^n)$ are likelihoods (weights) of particles that can be normalized to

$$
\omega_t^n = \frac{P(\chi_t | O_{t-1}^n)}{\sum_{n=1}^{N} P(\chi_t | O_{t-1}^n)} \qquad (12)
$$

Thus the expectation of β_t is given by

$$
\mathbb{E}\beta_t = \sum_{i=1}^{I} \omega_t^n O_t^n \qquad (13)
$$

□

Without loss of generality, one can draw particles from a prior distribution $\beta_0 \sim \mathcal{N}(\mu_0, v_0)$ at the initial time step. At the tth time step, $\mathbb{E}\beta_t$ equals to the weighted average of particles drew form $\beta_{t-1} \sim \mathcal{N}(\mu_{t-1}, v_{t-1})$. Nevertheless, the prior distribution is not always an unbiased estimation of the target. The weight of particles away from the expectation may degenerate into invalid values reducing the number of effective particles exponentially. The resampling technique is the crucial ingredient of SMC methods that (partially) solves this problem [31].

2. Resampling

Using the resampling procedure, the pOSL method replaces the degenerated particles by drawing repeated particles from the original particle set with survival probabilities determined by the weights [32,33]. One can firstly draw N samples from a uniform distribution $U_1 \sim U[0, (1/N)]$, and define $U_n = U_1 + (n-1)/N$ for $n = 2, \ldots, N$, then set $T^n = \left|U_j\right.$: $\sum_{k=1}^{n-1} \omega^k \le U_j \le \sum_{k=1}^{n} \omega^k\left|\right.$ with the convention $\sum_{k=1}^{0} \omega \coloneqq 0$. The resampling can be performed adaptively when the following inequality [Eq. (14)] holds:

$$
N_{\mathrm{eef}} = \frac{1}{\sum_{n=1}^{N} (\omega^n)^2} \le \frac{N}{2} \qquad (14)
$$

The variance of the particles set is reduced after resampling since the degenerated particles are replaced by copies of particles whose weights are greater.

3. Covariance Decay

We introduce a learning rate α given by Eq. (15) to decay the covariance of the likelihood function to increase its derivative around the source location and so further increase the targeting accuracy. As shown in Fig. 4, when particles are closing to O, we decrease the covariance of $P(\chi_t|O)$ to tilt the likelihood function and to maintain the diversity of weights. This increases the targeting accuracy.

$$
\begin{aligned}
&\Delta_t = \alpha \Delta_{t-1}, \\
&\alpha = e^{-\gamma n} \qquad (15)
\end{aligned}
$$

At the beginning of the descent, the particles are scattered around the prior guess, so that the likelihood function generates particles

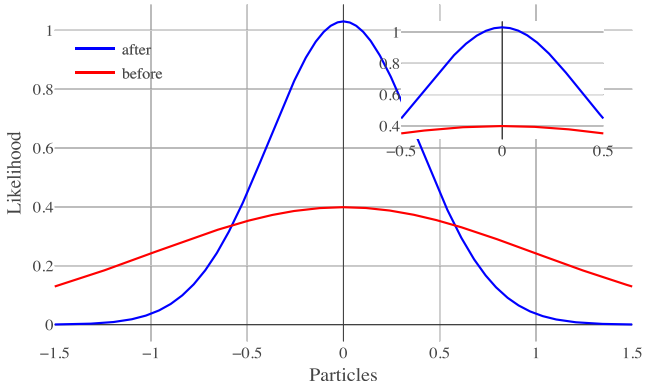

Fig. 4 The decay of the covariance. The derivative of the likelihood function near the source is larger when we decrease the covariance.

with diverse weights. However, when particles converge in a small area around the source, its weight may approach to $(1/N)$, since the derivative of the likelihood function trends to 0 near O. This reduces the diversity of the weights and restricts the convergence. The proposed covariance decay method increases the diversity of the particle set, which improves the estimated accuracy.

C. Framework of the Algorithm

Based on Eqs. (1), (11), (12), (13), and (9), Algorithm 1 determines estimates of the posterior distribution of the source requiring $O(N)$ operations per observation.

At the initial state of descent, pOSL draws N particles from a prior distribution $\mathcal{N}(O_0|\mu_0, V_0)$ and gives the first estimation as $O = (1/N)\sum_{n=1}^{N} O_0^n$. At every r_t, the algorithm evaluates the weights of every particle as $\omega_t^n \propto P(\chi_t|O_{t-1}^n)$. Then if $N_{\text{eff}} \leq (N/2)$, a new particle set $\{O_t\}^N$ with weights $\{1/N\}^N$ is generated by the resampling procedure. The posterior expectation of source location is updated by Eq. (13), imposing only $O(N)$ operations per observation. Compared with traditional methods, the pOSL method improves the overfitting and avoids the negative likelihood issue by implementing a novel probabilistic model that describes the observation likelihoods in the concentration function space.

Algorithm 1: pOSL algorithm

Data: $r_0, \chi_0, N, \mu_0, V_0, h$
Result: O
begin
  Initialize $t = 1$, $O_0^n \sim P(O)$;
  Initialize $O \coloneqq \frac{1}{N}\sum_{n=1}^{N} O_0^N$;
  while $h > 0$ **do**
    $P(\chi_t|O_{t-1}^n) \coloneqq \mathcal{N}(\chi_t; \mu_t, \alpha V_{t-1})$; $\omega_t^n \coloneqq P(\chi_t|O_{t-1}^n)$;
    $N_{\text{eff}} \coloneqq \frac{1}{\sum_{n=1}^{N}(\omega_t^N)^2}$;
    if $N_{\text{eff}} \leq \frac{N}{2}$ **then**
      $\{O_t\}^N \coloneqq$ resampling;
      $\{\omega_t\}^N \coloneqq \frac{1}{N}$;
    else
      $O_t^n \coloneqq O_{t-1}^n$;
    end
    $O \coloneqq \sum_{n=1}^{N} \omega_t^n O_t^n$;
    $\alpha \coloneqq e^{-\gamma t}$; $t \coloneqq t + 1$;
    Update the reference trajectory;
    Read r_t and χ_t;
  end
end

The pOSL algorithm enables an Enceladus lander to locate the plume source autonomously by sniffing the plume during its descent. According to [14], we assumed a penetrator mission with the desired impact velocity of 162 $\text{m} \cdot \text{s}^{-1}$ into the surface ice following a conical search profile of 90 km diameter at its widest. The simulation results demonstrate that by performing pOSL, the penetrator could locate the plume vents and impact one.

IV. Simulation Studies

A. Simulation of an Enceladus Penetrator Mission

The baseline simulations were performed in an inertial coordinate system whose origin is an assumed plume source located at the south pole of Enceladus. We applied a penetrator mission concept according to Sun et al. [14], where a 12 kg penetrator explores the plume environment by exploiting vectoring-in-forward-flight (viffing): a series of lateral maneuvers while autonomously locating the plume source during the descent through the plume. The penetrator free falls from Enceladus's sphere of influence (at 208 km altitude) with 0 $\text{m} \cdot \text{s}^{-1}$ initial velocity in order to penetrate the icy crust near a plume vent and deploy its scientific instruments into it. Ideally, the free-falling penetrator would impact the ice shell at ~162 $\text{m} \cdot \text{s}^{-1}$, which guarantees an effective penetration depth of ~0.2–1 m depending on the ice hardness. The penetrator explores the plume field based on [34] through a lateral corridor of 90 km diameter by passing through a sequence of descending reference waypoints. During the descent, the penetrator measures the plume every 0.1 s and updates the reference waypoints every 1s by inferring the source location based on the pOSL method.

The penetrator explores the plume environment by performing a biomimetic strategy, the quasi-spiral descent (Fig. 5). During the free fall, the lander passes through a sequence of arbitrary waypoints to approximate a logarithmic spiral in the lateral direction, which mimics the phototaxis behavior of moths [35–37]. According to Sun et al. [14], the quasi-spiral trajectory achieves the most fuel efficiency in searching the plume environment compared with other trajectories. During the descent, the penetrator locates the plume source via pOSL and then updates the remaining waypoint positions until impact. Assuming that the source location is known a priori approximately, we first give a reference trajectory and the corresponding waypoint positions, but these are updated as the trajectory proceeds. The maneuver ΔV costs of each waypoints are listed in Table 1. This simulation is performed using the astrogator toolbox of Satellite Toolkit (STK) with an Enceladus-centric reference frame.

B. Offline Simulations of pOSL

Before the online mapping scenario, we performed an offline simulation using plume data accumulated during the reference trajectory to compare the pOSL algorithm and the particle-filter-based method [28]. The prior source distribution was assumed to be a uniform distribution across an area of 50 km × 50 km.

To avoid negative weights generated by the particle-filter-based method, we normalized the likelihoods before computing the undetected weights. From Fig. 6, the estimation is made to follow the search trajectory of the penetrator. Figure 6 illustrates that the particle-filter-based algorithm is affected by the vehicle position sequence implying very strong overfitting and even impacting the convergence of the algorithm. If the penetrator detects $\chi_t = 1$ at r_t that is far away from the source, the traditional algorithm gives an estimation near r_t, rather than O. Also, if the penetrator detects $\chi_t = 0$ near the source, the algorithm may give an estimation that is far away from the source. Figure 6 also illustrates that the estimation converges to the source only if the vehicle is in a narrow area near it. However, the impact velocity of a landing vehicle is required to be near 100 ~ 300 $\text{m} \cdot \text{s}^{-1}$ to guarantee a sufficient impact depth, leaving little room for lateral maneuvers to alter the impact target.

The following simulation demonstrates that pOSL resolves the NLO issue. During the quasi-spiral descent, the estimations given by pOSL (shown in Fig. 7) are always in a narrow area around the source, rather than oscillating with the search trajectory like the particle-

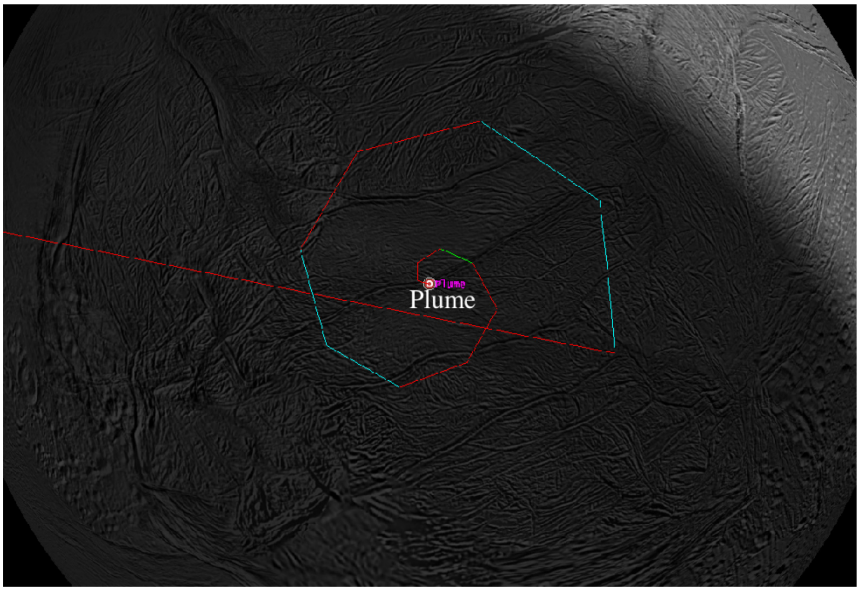

Fig. 5 Quasi-spiral trajectory above the plume area of Enceladus. Trajectory segments are distinguished by different colors.

Table 1 Maneuver summary of the quasi-spiral trajectory with duration from release, waypoint positions and altitudes, penetrator velocity at waypoints, ΔV costs, and fuel consumption

Waypoint number	Waypoint position (km)	Waypoint velocity ($m \cdot s^{-1}$)	Altitude (km)	ΔV ($m \cdot s^{-1}$)	Fuel used (kg)
1	(42, 42, −456)	(32, −75, 0)	208	81.76	0
2	(60, 0, −450.4)	(−49, −93, 19.6)	206	81.19	0.50
3	(39, −39, −439)	(−105, −30, 34)	194	82.67	0.48
4	(0, −50, −423.4)	(−101.6, 56, 49)	178	85.58	0.48
5	(−32, −32, −406)	(−31.5, 124, 62)	160	96.39	0.48
6	(−40, 0, −388)	(67, 113, 74)	142	98.51	0.53
7	(−25, 25, −371)	(97, 20, 85)	124	97.22	0.52
8	(0, 30, −347)	(119, −79, 99)	100	100.49	0.49
9	(18, 18, −331)	(11, −92, 109)	84	109.15	0.49
10	(20, 0, −309)	(−76, −86, 122)	61	85.72	0.52
11	(10, −10, −292)	(−91, 5.6, 132)	45	92.47	0.39
12	(0, −10, −277)	(−33, 59.5, 142)	29	78.95	0.41
13	(−4, −4, −261)	(43, 43, 152)	13	77.78	0.34
14	(−1, −1, −251)	(43, 43, 159)	0.1	20.51	0.33
Target	(0, 0, −248)	(0, 0, 162)	0	85.15	0.25
Summary				1228.4	6.22

The waypoint positions and velocities are referred to inertial coordinates.

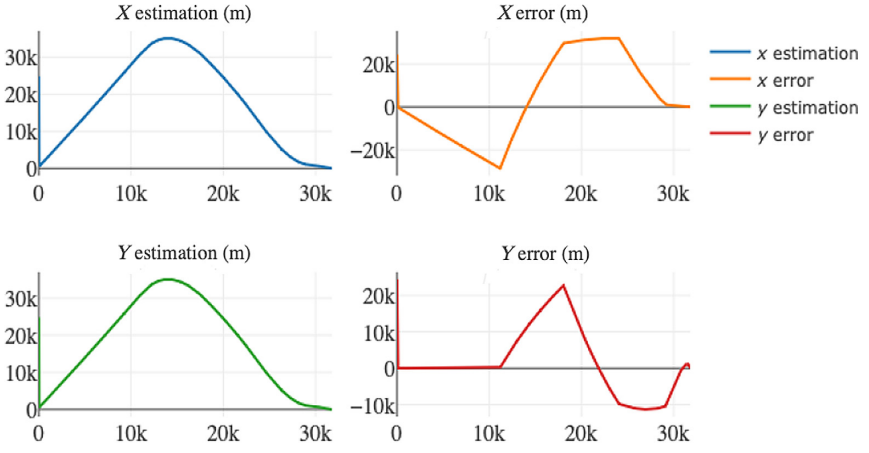

Fig. 6 Horizontal estimations of the particle-filter-based method, including estimations and errors in x and y directions.

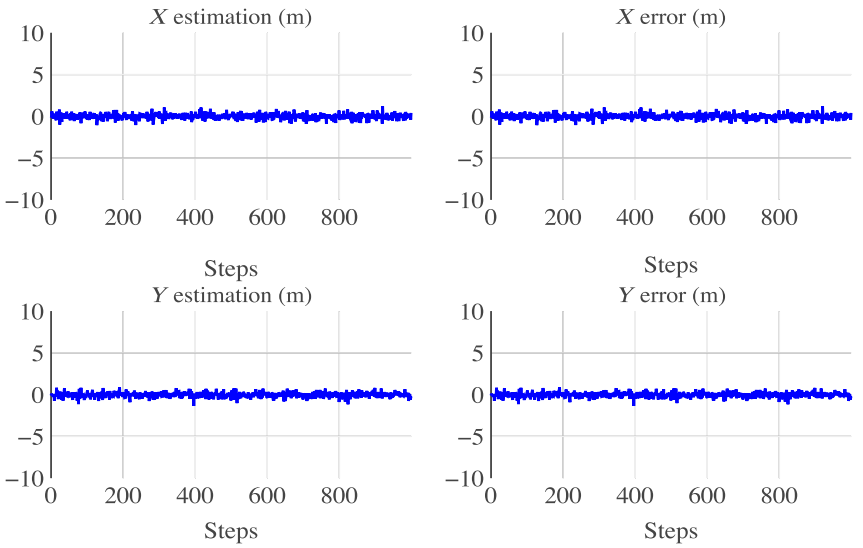

Fig. 7 Estimation trajectories of pOSL in the horizontal plane, including estimations and errors in x and y directions.

based method. Therefore, pOSL reduces the overfitting caused by the likelihood function while enabling the penetrator to locate the plume source in a large lateral search area of 90°.

The employment of Monte Carlo targeting with 1000 runs using a residual from [34] and observation noises ($\Gamma = 2$ or 5) are shown in the first row of Fig. 8. The average and the ℓ^2 norm of targeting error are listed in the first two columns of Table 2. The ℓ^2 norm of estimation error is 0.19 m when $\Gamma = 5$ and 0.12 m when $\Gamma = 2$, which is extremely small compared with the search area. By implementing pOSL algorithm, the error of source localization is reduced from 416.66 m at the beginning of the descent to $0.12 \sim 0.19$ m at the impact. This reveals that the proposed algorithm permits accurate targeting of the plume source, even when the prior knowledge about the source location is inaccurate.

The following simulation demonstrates that the introduction of the covariance decay method improves the estimation accuracy. The second row of Fig. 8 and the last two columns of Table 2 show 1000 runs Monte Carlo targeting with a decay rate $\gamma = 0.01$. The ℓ^2 norm of target error is reduced by 40.8% when $\Gamma = 2$ and 27.2% when $\Gamma = 5$. The accuracy of targeting is improved after introducing the proposed learning rate, which demonstrates the effectiveness of the covariance decay method.

C. Online Simulation

Assuming that the prior guess of the source is (1, 1, 0) km, 300 runs Monte Carlo targeting with online plume source localization via pOSL are shown in the first column of Fig. 9. The penetrator updates the remaining waypoint positions based on the estimated source

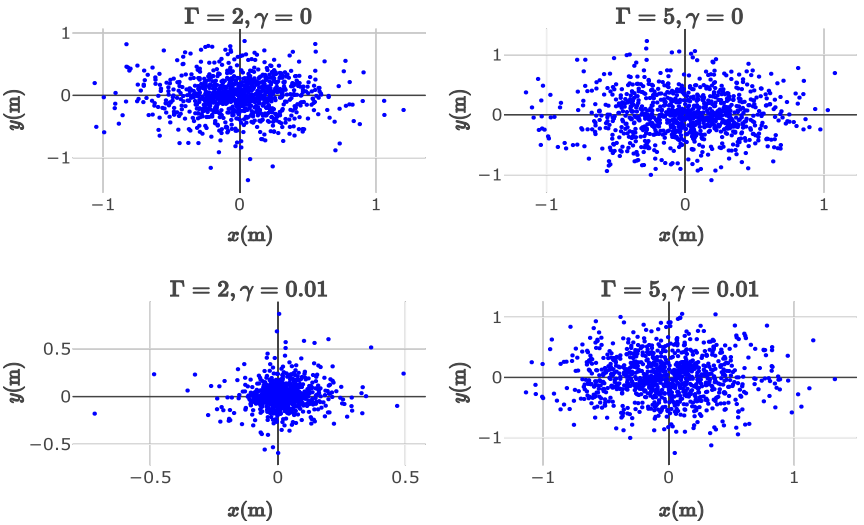

Fig. 8 Offline Monte Carlo simulation considering different observation noise ($\Gamma = 2.5$ or 5) and different learning rate ($\gamma = 0$ or 0.01).

Table 2 Simulation results of the offline algorithm under different observation noise ($\Gamma = 2$ or 5) and different decay rates ($\gamma = 0$ or 0.01) of the learning rate

Parameter	$\Gamma = 2, \gamma = 0$	$\Gamma = 5, \gamma = 0$	$\Gamma = 2, \gamma = 0.01$	$\Gamma = 5, \gamma = 0.01$
Average of landing sites	[−0.005, −0.01]	[−0.02, 0.009]	[0.001, 0.008]	[−0.01, −0.003]
ℓ^2 of landing sites	0.19	0.12	0.11	0.08

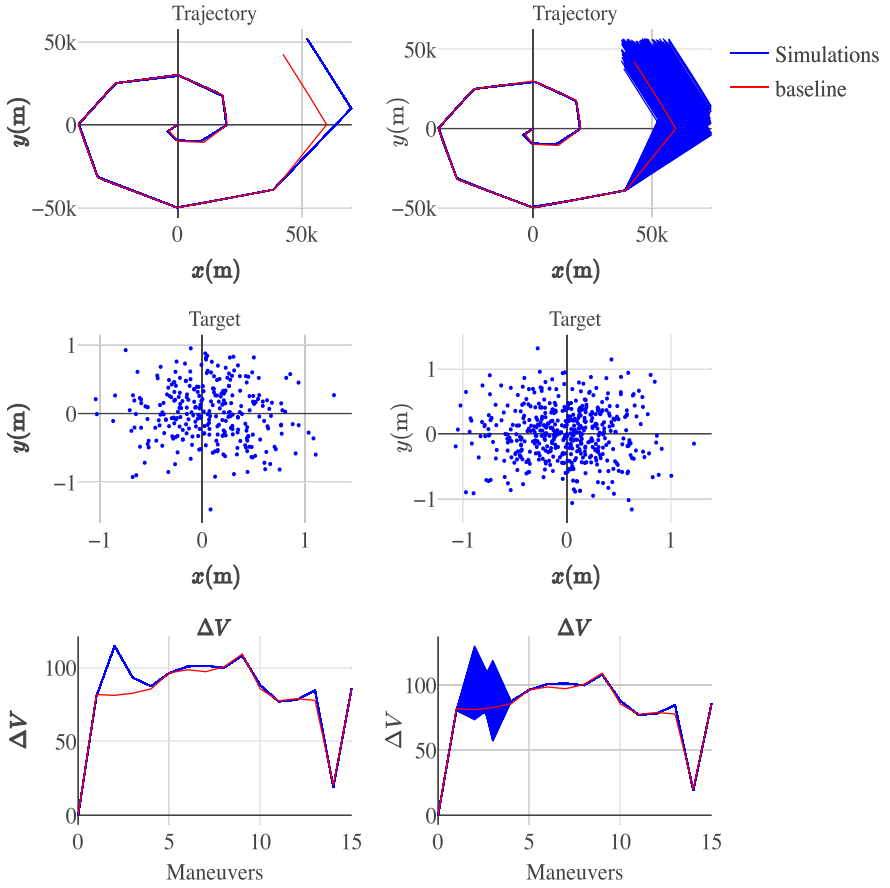

Fig. 9 Monte Carlo targeting of online plume source localization with no initial state noise (the left column) and an initial state noise of $\mathcal{N}(420, 500)$ (the right column), showing the lateral trajectory, target sites, and maneuver ΔV.

Table 3 Summary of both fixed initial state and random initial, showing the mean values of target error, the covariances of target error, the mean values of ΔV, and the covariances of ΔV

Scenario	Average target error (m)	ℓ^2 of target error	Average ΔV ($\mathrm{m} \cdot \mathrm{s}^{-1}$)	ℓ^2 of ΔV
Fixed initial states	[−0.018, 0.009]	0.14	1314.14	0.004
Random initial states	[0.07, 0.008]	0.16	1294.58	293.03

location during the descent. Maneuver ΔV costs are listed in the first row of Table 3. The average ΔV cost of the Monte Carlo targeting is 1314.14 $\mathrm{m} \cdot \mathrm{s}^{-1}$ with a covariance of 0.004. Compared with the baseline in which the plume source is known a priori, the additional ΔV is ∼85.75 $\mathrm{m} \cdot \mathrm{s}^{-1}$, implying that the penetrator only imposes a 6.98% ΔV increase to eliminate the estimation error of the source location. Only the first three waypoints have significant ΔV discrepancy, yet the remaining waypoints have almost the same ΔV costs compared with the baseline Table 1. This illustrates that pOSL could locate the plume source position very fast.

We now input a Gaussian noise $\mathcal{N}(420, 500)$ into the initial state of the descent and a uniform noise $U[-5, 15]$ km into the prior guess of the source location. The trajectory ΔV costs and impact sites of 500 runs of Monte Carlo targeting are shown in the second column of Fig. 9 and the second row of Table 3, respectively. After the second waypoint, the simulation trajectories almost overlap with the reference, implying that the pOSL algorithm converges to the source localization very fast even with different initial states. This demonstrates that the pOSL algorithm could eliminate the observation noise and systemic noise effectively. Thus the proposed algorithm enables the penetrator to map the plume autonomously and target it source accurately.

Figure 10 shows the top view and the lateral view of the decent trajectory guided by pOSL in the concentration field. The penetrator explores the plume environment through a lateral quasi-spiral trajectory, and locates the source via pOSL autonomously during the descent; this represents a biomimetic plume sniffing behavior.

V. Conclusions

To investigate the potential astrobiological environment of Enceladus, this paper proposes a method that enables a lander to map the plume and locate its vent autonomously during the descent even when the prior knowledge about the source location is inaccurate. By defining the observation value as the latent variable, the proposed algorithm evaluates the observation likelihood distribution via the posterior maximization method instead of the likelihood maximization method that eliminates the deficiencies of traditional algorithms. The proposed method also permits accurate targeting of the plume vent with a linear computational complexity and modest ΔV costs. In the case of resource-constrained penetrators that employ limited computational hardware capacity, this is a crucial issue. This approach, although discussed in terms of a penetrator mission, is directly applicable to any life-detection mission to Enceladus. The proposed method also offers the best chance for targeting the plume vent source to maximize access to pristine samples from the subsurface ocean for astrobiological investigation.

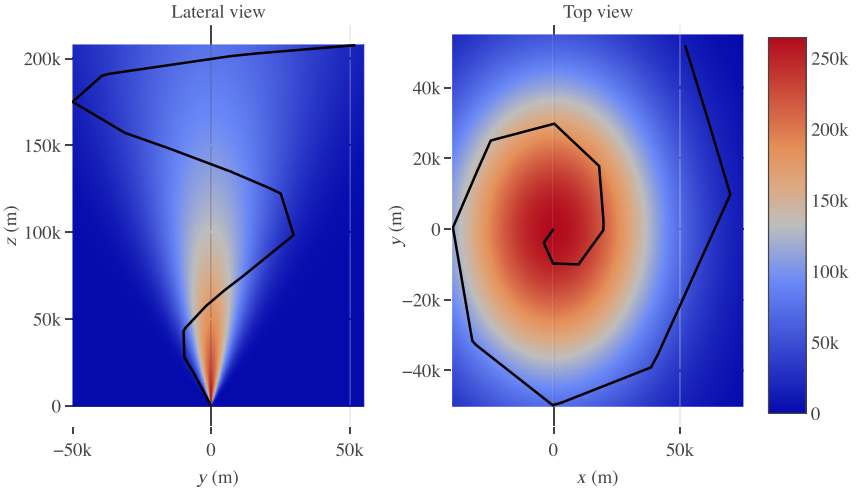

Fig. 10 Enceladus plume mapping trajectory (black line), where the color contour represents the plume flowfield.

References

[1] Geissler, P., "Cryovolcanism in the Outer Solar System," *The Encyclopedia of Volcanoes*, Elsevier, Amsterdam, 2015, pp. 763–776.

[2] Domagal-Goldman, S. D., Wright, K. E., Adamala, K., Arina de la Rubia, L., Bond, J., Dartnell, L. R., Goldman, A. D., Lynch, K., Naud, M.-E., Paulino-Lima, I. G., Singer, K., Walter-Antonio, M., Abrevaya, X. C., Anderson, R., Arney, G., Atri, D., Azúa-Bustos, A., Bowman, J. S., Brazelton, W. J., Brennecka, G. A., Carns, R., Chopra, A., Colangelo-Lillis, J., Crockett, C. J., DeMarines, J., Frank, E. A., Frantz, C., de la Fuente, E., Galante, D., Glass, J., Gleeson, D., Glein, C. R., Goldblatt, C., Horak, R., Horodyskyj, L., Kaçar, B., Kereszturi, A., Knowles, E., Mayeur, P., McGlynn, S., Miguel, Y., Montgomery, M., Neish, C., Noack, L., Rugheimer, S., Stüeken, E. E., Tamez-Hidalgo, P., Walker, S. I., and Wong, T., "The Astrobiology Primer v2.0," *Astrobiology*, Vol. 16, No. 8, 2016, pp. 561–653. https://doi.org/10.1089/ast.2015.1460

[3] Postberg, F., Schmidt, J., Hillier, J., Kempf, S., and Srama, R., "A Salt-Water Reservoir as the Source of a Compositionally Stratified Plume on Enceladus," *Nature*, Vol. 474, No. 7353, 2011, pp. 620–622. https://doi.org/10.1038/nature10175

[4] Porco, C. C., "Cassini Observes the Active South Pole of Enceladus," *Science*, Vol. 311, No. 5766, 2006, pp. 1393–1401. https://doi.org/10.1126/science.1123013

[5] Waite, J. H., "Cassini Ion and Neutral Mass Spectrometer: Enceladus Plume Composition and Structure," *Science*, Vol. 311, No. 5766, 2006, pp. 1419–1422. https://doi.org/10.1126/science.1121290

[6] Krupp, N., Roussos, E., Kollmann, P., Paranicas, C., Mitchell, D., Krimigis, S., Rymer, A., Jones, G., Arridge, C., Armstrong, T., and Khurana, K., "The Cassini Enceladus Encounters 2005–2010 in the View of Energetic Electron Measurements," *Icarus*, Vol. 218, No. 1, 2012, pp. 433–447. https://doi.org/10.1016/j.icarus.2011.12.018

[7] Lee, A., Wang, E., Pilinski, E., Macala, G., and Feldman, A., "Estimation and Modeling of Enceladus Plume Jet Density Using Reaction Wheel Control Data," *AIAA Guidance, Navigation, and Control Conference*, AIAA Paper 2010-7563, 2010.

[8] Witze, A., "Icy Enceladus Hides a Watery Ocean," *Nature*, 2014.

[9] Barge, L. M., and White, L. M., "Experimentally Testing Hydrothermal Vent Origin of Life on Enceladus and Other Icy/Ocean Worlds," *Astrobiology*, Vol. 17, No. 9, 2017, pp. 820–833. https://doi.org/10.1089/ast.2016.1633

[10] Porco, C. C., Dones, L., and Mitchell, C., "Could It Be Snowing Microbes on Enceladus? Assessing Conditions in Its Plume and Implications for Future Missions," *Astrobiology*, Vol. 17, No. 9, 2017, pp. 876–901. https://doi.org/10.1089/ast.2017.1665

[11] Hargitai, H., and Kereszturi, Á., *Encyclopedia of Planetary Landforms*, 1st ed., Springer-Verlag, New York, 2015, pp. 105–119.

[12] Szumski, A., Konstantinidis, K., Förstner, R., and Eissfeller, B., "Enceladus' Environment and the Design of the Enceladus Ice-Probe Navigation System," *AIAA SPACE 2016*, AIAA Paper 2016-5536, 2016.

[13] Russell, R. P., and Strange, N. J., "Cycler Trajectories in Planetary Moon Systems," *Journal of Guidance, Control, and Dynamics*, Vol. 32, No. 1, 2009, pp. 143–157. https://doi.org/10.2514/1.36610

[14] Sun, Y., Ellery, A., and Huang, X., "Targeting the Geysers on Enceladus by Viffing Descent Through the Icy Plumes," *Advances in Space Research*, Vol. 65, No. 7, 2020, pp. 1863–1876.

[15] Lo, A., Eller, H., and Sollitt, L., "Penetrator Science—Making an Impact on Planetary Compositional Science," *Space 2006*, AIAA Paper 2006-7423, 2006.

[16] Lorenz, R. D., "Planetary Penetrators: Their Origins, History and Future," *Advances in Space Research*, Vol. 48, No. 3, 2011, pp. 403–431. https://doi.org/10.1016/j.asr.2011.03.033

[17] Yang, Gao, Ellery, A., Jaddou, M., Vincent, J., and Eckersley, S., "Planetary Micro-Penetrator Concept Study with Biomimetric Drill and Sampler Design," *IEEE Transactions on Aerospace and Electronic Systems*, Vol. 43, No. 3, 2007, pp. 875–885. https://doi.org/10.1109/TAES.2007.4383580

[18] Tuckness, D. G., "Precision Landing on Mars Using Imaging Penetrator Beacons," *Journal of Spacecraft and Rockets*, Vol. 31, No. 6, 1994, pp. 1085–1091. https://doi.org/10.2514/3.26563

[19] Tuckness, D. G., "Imaging Penetrator-Beacon Design for Mars," *Journal of Spacecraft and Rockets*, Vol. 31, No. 6, 1994, pp. 1123–1129. https://doi.org/10.2514/3.26568

[20] Hansen, C. J., "Enceladus' Water Vapor Plume," *Science*, Vol. 311, No. 5766, 2006, pp. 1422–1425. https://doi.org/10.1126/science.1121254

[21] Lilienthal, A., Loutfi, A., and Duckett, T., "Airborne Chemical Sensing with Mobile Robots," *Sensors*, Vol. 6, No. 11, 2006, pp. 1616–1678. https://doi.org/10.3390/s6111616

[22] Grasso, F. W., Consi, T. R., Mountain, D. C., and Atema, J., "Biomimetic Robot Lobster Performs Chemo-Orientation in Turbulence Using a Pair of Spatially Separated Sensors: Progress and Challenges," *Robotics and Autonomous Systems*, Vol. 30, Nos. 1–2, 2000, pp. 115–131. https://doi.org/10.1016/S0921-8890(99)00068-8

[23] Vergassola, M., Villermaux, E., and Shraiman, B. I., "'Infotaxis' as a Strategy for Searching Without Gradients," *Nature*, Vol. 445, No. 7126, 2007, pp. 406–409. https://doi.org/10.1038/nature05464

[24] Russell, R., Bab-Hadiashar, A., Shepherd, R. L., and Wallace, G. G., "A Comparison of Reactive Robot Chemotaxis Algorithms," *Robotics and Autonomous Systems*, Vol. 45, No. 2, 2003, pp. 83–97. https://doi.org/10.1016/S0921-8890(03)00120-9

[25] Ferri, G., Caselli, E., Mattoli, V., Mondini, A., Mazzolai, B., and Dario, P., "SPIRAL: A Novel Biologically-Inspired Algorithm for Gas/Odor Source Localization in an Indoor Environment with No Strong Airflow," *Robotics and Autonomous Systems*, Vol. 57, No. 4, 2009, pp. 393–402. https://doi.org/10.1016/j.robot.2008.07.004

[26] Hayes, A. T., Martinoli, A., and Goodman, R. M., "Swarm Robotic Odor Localization: Off-Line Optimization and Validation with Real Robots," *Robotica*, Vol. 21, No. 4, 2003, pp. 427–441. https://doi.org/10.1017/S0263574703004946

[27] Farrell, J., Shuo, P., and Wei, L., "Plume Mapping via Hidden Markov Methods," *IEEE Transactions on Systems, Man and Cybernetics, Part B (Cybernetics)*, Vol. 33, No. 6, 2003, pp. 850–863. https://doi.org/10.1109/TSMCB.2003.810873

[28] Li, J.-G., Meng, Q.-H., Wang, Y., and Zeng, M., "Odor Source Localization Using a Mobile Robot in Outdoor Airflow Environments with a Particle Filter Algorithm," *Autonomous Robots*, Vol. 30, No. 3, 2011,

pp. 281–292.
https://doi.org/10.1007/s10514-011-9219-2

[29] Yun, S., and Zanetti, R., "Sequential Monte Carlo Filtering with Gaussian Mixture Sampling," *Journal of Guidance, Control, and Dynamics*, Vol. 42, No. 9, 2019, pp. 2069–2077.
https://doi.org/10.2514/1.G004403

[30] Bishop, C. M., *Pattern Recognition and Machine Learning, Information Science and Statistics*, Springer, New York, 2006, pp. 85–93.

[31] Fearnhead, P., Wyncoll, D., and Tawn, J., "A Sequential Smoothing Algorithm with Linear Computational Cost," *Biometrika*, Vol. 97, No. 2, 2010, pp. 447–464.
https://doi.org/10.1093/biomet/asq013

[32] Del Moral, P., Doucet, A., and Jasra, A., "On Adaptive Resampling Strategies for Sequential Monte Carlo Methods," *Bernoulli*, Vol. 18, No. 1, 2012, pp. 252–278.
https://doi.org/10.3150/10-BEJ335

[33] Douc, R., and Cappe, O., "Comparison of Resampling Schemes for Particle Filtering," *ISPA 2005. Proceedings of the 4th International Symposium on Image and Signal Processing and Analysis, 2005*, Inst. of Electrical and Electronics Engineers, New York, 2005, pp. 64–69.

[34] Saur, J., Schilling, N., Neubauer, F. M., Strobel, D. F., Simon, S., Dougherty, M. K., Russell, C. T., and Pappalardo, R. T., "Evidence for Temporal Variability of Enceladus' Gas Jets: Modeling of Cassini Observations," *Geophysical Research Letters*, Vol. 35, No. 20, 2008, pp. 433–447.
https://doi.org/10.1029/2008GL035811

[35] Pyk, P., Bermúdez i Badia, S., Bernardet, U., Knüsel, P., Carlsson, M., Gu, J., Chanie, E., Hansson, B. S., Pearce, T. C., and Verschure, P. F. M. J., "An Artificial Moth: Chemical Source Localization Using a Robot Based Neuronal Model of Moth Optomotor Anemotactic Search," *Autonomous Robots*, Vol. 20, No. 3, 2006, pp. 197–213.
https://doi.org/10.1007/s10514-006-7101-4

[36] López, L., Vouloutsi, V., Escuredo, A., Marcos, E., i Badia, S. B., Mathews, Z., Verschure, P. F. M. J., Ziyatdinov, A., and i Llu, A. P., "Moth-Like Chemo-Source Localization and Classification on an Indoor Autonomous Robot," *On Biomimetics*, edited by L. Pramatarova, InTech, London, 2011, pp. 454–463.

[37] Gonzalez, E., Mascenon, F., Magpantay, A., Go, K., and Cordero, M., "Design of an Autonomous Mobile Olfactory Robot for Chemical Source Localization," *2004 IEEE Region 10 Conference TENCON 2004*, Vol. D, Inst. of Electrical and Electronics Engineers, New York, 2004, pp. 475–478.

J. McMahon
Associate Editor